Why does El Niño tend to peak in boreal winter: I. the role of the ocean-atmosphere coupling strength

Lunyu Li[1,2], De-Zheng Sun[3], and Wen Zhou[1, 2]

[1]Department of Atmospheric and Oceanic Sciences & Institute of Atmospheric Sciences, Fudan University, Shanghai, China. [2]Key Laboratory for Polar Science of the MNR, Polar Research Institute of China, Shanghai, China. [3]Nanjing-Helsinki Institute in Atmospheric and Earth System Sciences, Nanjing University-Suzhou Campus, Suzhou, Jiangsu, China.

Corresponding author: D. Z., Sun and W. Zhou, dezheng.sun@nju.edu.cn; Wen_zhou@fudan.edu.cn

Key Points:

- El Niño peaking in boreal winter is caused by the seasonal cycle of the ocean-atmosphere coupling strength
- The strength of phase-locking is influenced by the amplitude of the coupling strength seasonal cycle through nonlinear frequency locking
- The peak time of El Niño is determined by the phase of the seasonal cycle of the coupling strength between the atmosphere and ocean

Abstract

This study investigates the seasonal phase-locking of El Niño peaks using the model of Sun (1997) that well simulates various characteristics of ENSO. Our findings reveal that when the dynamical coupling strength between the atmosphere and ocean in the model varies seasonally, as observed, El Niño events tend to peak during boreal winter. The extent of this phase-locking is influenced by the amplitude of the coupling strength seasonal cycle through the nonlinear frequency locking. In observations, El Niño peaks in winter because the coupling strength is highest in October and lowest in April. The time lag between the peak coupling strength and the peak El Niño magnitude is related to the amplitude of the seasonal cycle in the coupling strength. Furthermore, we found the higher coupling strength in the seasonal cycle may correspond to a higher ENSO growth rate by calculating the seasonal cycle of the model equilibriums.

Plain Language Summary

Observations show that El Niño events, which have significant global impacts, tend to reach their peak intensity during the Northern Hemisphere winter, from November to January. This phenomenon is known as the seasonal phase-locking of El Niño. In this study, we use a nonlinear theoretical model to explore the causes for this phase-locking. Our findings reveal that the coupling strength between the ocean and atmosphere in the tropical Pacific is highest in fall and lowest in spring, which causes El Niño events to peak in winter. This research is important for better understanding and simulating the seasonal phase-locking of El Niño.

1 Introduction

The El Niño–Southern Oscillation (ENSO) is the dominant mode of interannual variability in the tropical Pacific with global impacts (Cheung et al., 2021; Jian et al., 2021; Leung & Zhou, 2016; Tu et al., 2022; Wang et al., 2014; Zhang et al., 2022). A key feature of El Niño is its boreal winter peak phase-locking to November-January (Hirst, 1986; Philander et al., 1984). However, the governing mechanism remains unclear.

The seasonal cycle in ocean-atmosphere coupling strength is proposed to be a critical factor in El Niño peak phase-locking (Galanti & Tziperman, 2000; Timmermann et al., 2003; Tziperman et al., 1998). Galanti & Tziperman (2000) and Tziperman et al. (1998) incorporated the coupling strength (the linear regression coefficient of the equatorial central Pacific zonal wind response to the Niño-3 sea surface temperature anomalies (SSTA)) seasonal cycle with summer maxima and winter minima into the delayed oscillator mechanism and showed that the seasonally varying amplification of the oceanic Rossby and Kelvin waves by the coupling strength forces El Niño events to peak in boreal winter when this amplification is minimum. However, the seasonal cycle is calculated from the model of Zebiak and Cane (1987) and is inconsistent with observations. Timmermann et al. (2003) incorporated seasonally varying coupling strength of similar definition into the nonlinear theoretical model which is also used in this study. However, their research focused on the ENSO decadal variability and did not address the issue of the seasonal phase-locking. Therefore, the real role of coupling strength in seasonal phase-locking remains unsettled.

Within the recharge oscillator framework, studies (Chen & Jin, 2020, 2022; Lu & Liu, 2019; Stein et al., 2010, 2014; Zheng et al., 2024) attribute phase-locking to seasonal variations in ENSO growth rates, with autumn maxima/spring minima, thus forcing El Niño to peak in boreal winter. The declining growth rate from autumn to spring further contributes to the spring persistence barrier of ENSO (Jin et al., 2019). While researches have not reached a consensus on the primary dynamical drivers of the seasonally varying growth rate, the atmospheric thermal damping coefficient is widely recognized to play an important role (Chen & Jin, 2022; Jin et al., 2019). Thus, the damping coefficient also may be a critical factor in the phase-locking. Yu et al. (2024) utilized the model of Sun (1997) (used in this work) to investigate the roles of observational seasonal cycles of damping coefficient and dynamical coupling between zonal SST gradients and upwelling in the eastern Pacific in ENSO spring prediction barrier from the perspective of ENSO's chaotic characteristics. This work has provided new insights to the investigation on the role of damping coefficient in the phase-locking.

Another mechanism proposed for the phase-locking is the nonlinear frequency locking of ENSO to the seasonal cycle (Jin et al., 1994, 1996; Stein et al., 2014). The phase-locking originates in frequency-locked oscillations with ENSO frequency locked to a rational multiple of the annual cycle under external annual forcing. However, it is unclear which factor dominates phase-locking and why El Niño peaks are locked in boreal winter.

This research uses the ENSO model of Sun (1997) to investigate the phase-locking. The model is simple to enable sensitivity experiments on parameters and captures key physical processes associated with ENSO. We investigate the roles of the coupling strength and the atmospheric thermal damping coefficient in the phase-locking, and part I shows the results of coupling strength. The seasonal cycle is calculated from different datasets and incorporated into the model to analyze its role in the phase-locking. Amplitude/phase sensitivity experiments of the seasonal cycle are conducted to analyze factors determining the strength and peak-time of phase-locking, as well as the phase-locking mechanism. The linkage between seasonal cycles of coupling strength and ENSO growth rate is discussed. The role of atmospheric thermal damping will be in Part II.

2 Methods and Data

2.1 The model of Sun (1997) with seasonal cycle

Equations 1-6 show the original model equations, and Equation 7 shows the introduced seasonal cycle.

$$\frac{dT_1}{dt} = c(T_e - T_1) + sq(T_2 - T_1) \tag{1}$$

$$\frac{dT_2}{dt} = c(T_e - T_2) + q(T_{sub} - T_2) \tag{2}$$

$$q = \frac{\alpha}{a}(T_1 - T_2) \tag{3}$$

$$T_{sub}\left(h_2'\right)=T_e-\frac{T_e-T_b}{2}\left[1-\tanh\left(\frac{h_2'-H_1+z_0}{H^*}\right)\right] \quad (4)$$

$$\frac{1}{r}\frac{dh_1'}{dt}=-h_1'+\frac{H_1}{2H_2}H\frac{\alpha}{b^2}(T_1-T_2) \quad (5)$$

$$h_2'-h_1'=-\frac{H_1}{H_2}H\frac{\alpha}{b^2}(T_1-T_2) \quad (6)$$

$$\alpha=\alpha_0\left(1+\Delta\sin\left(\omega_y t+\varphi\right)\right) \quad (7)$$

Equations 1-2 are forecast equations for the tropical Pacific SST. T_1 and T_2 respectively represent SST in the Western and Eastern Pacific (WP and EP). T_e is the radiative-convective equilibrium temperature of the tropical Pacific. Parameter *c* is the atmospheric thermal damping coefficient. In Equation 3, *q* measures the upwelling strength, and *α* is the dynamical ocean-atmosphere coupling strength and measures the sensitivity of wind stress to changes in zonal SST gradients. Surface wind stress is assumed to be proportional to the zonal SST gradients and the ocean currents strength is proportional to the surface wind stress (Sun & Liu, 1996). Subsurface temperature T_{sub} is a function of the thermocline depth (Equation 4); h_1' and h_2' are respectively the deviations of WP and EP thermocline depth from its reference depth. The thermocline depths are governed by Equations 5 and 6, which follow Jin (1996). Detailed descriptions and definitions of the model variables and parameters are in the Supporting Information Text S1 and Table S1.

For the coupling strength seasonal cycle (Equation 7), we use the sine function to approximate the observational seasonal cycle; Δ is the amplitude of the seasonal cycle relative to/divided by the annual mean α_0; ω_y is the frequency of the seasonal cycle; φ is the phase determining the months of the maximum/minimum coupling strengths. The seasonal variation of coupling strength influences the system in two ways: one is the zonal SST gradients-zonal wind stress-ocean currents positive feedback (Equation 3). The other is the role of wind stress in modulating thermocline depth (Equations 5-6) (Philander, 1989). The annual mean state is set as: T_e=31℃, T_b=17.3℃, $1/c$=150 days, $1/r$=300 days, H^*=65 m, H_1=50 m, H_2=150 m, z_0=75 m, $\alpha_0/a=3*10^{-8}$ K^{-1} s^{-1}, $H_1H\alpha_0/H_2b^2$=23 mK^{-1}, the same as Figure 5 in Liang et al. (2012). For the seasonal cycle, $\omega_y=2\pi/365$ day^{-1}, we will show that Δ≈0.5, $\varphi=335\pi/365$, meaning the maximum/minimum coupling strength in October/April. In each experiment, the model is run for 3000 years with 1.5-day time step. We calculate the monthly mean of results from the latter 2000 years and calculate the interannual anomalies by removing the climatology in each month. El Niño events are defined as occurring when EP SST (T_2) anomalies exceed +1.0 standard deviation.

2.2 Observations

The monthly SST is from the Hadley Centre Global Sea Ice and Sea Surface Temperature dataset (HadISST; Rayner et al., 2003) during 1870-2023. The phase-locking in the Niño-3.4 region (5°S–5°N, 190°-240°E) in the observations is analyzed. An El Niño event is defined as occurring when the 3-month running averaged SSTA index exceeds +1.0 standard deviation. The anomalies are based on the climatology of the dataset period.

The zonal wind stress from four datasets are used: 1) NCEP-NCAR Reanalysis 1 (Kalnay et al., 1996) during 1948-2023; 2) The fifth-generation ECMWF atmospheric reanalysis of the global climate (ERA5, Hersbach et al., 2020) during 1948-2023; 3) the Global Ocean Data Assimilation System (GODAS; Behringer et al., 1998) during 1980-2023; and 4) the Simple Ocean Data Assimilation (SODA) 3.15.2 dataset (Carton et al., 2018) during 1980-2023. When calculating the coupling strength for a particular month, we linearly regress the monthly mean interannual anomalies of the zonal wind stress in the central equatorial Pacific (5°S-5°N, 160°-200°E) to the corresponding variations in the equatorial zonal SST contrast calculated from the HadISST dataset (Sun, 2003; Sun et al., 2004). The contrast is defined as the area-averaged SST difference between (5°S–5°N, 130°E–180°) and (5°S–5°N, 230°-280°E).

3 Results

3.1 Observed phase-locking of El Niño peaks and seasonal cycle in ocean-atmosphere coupling strength

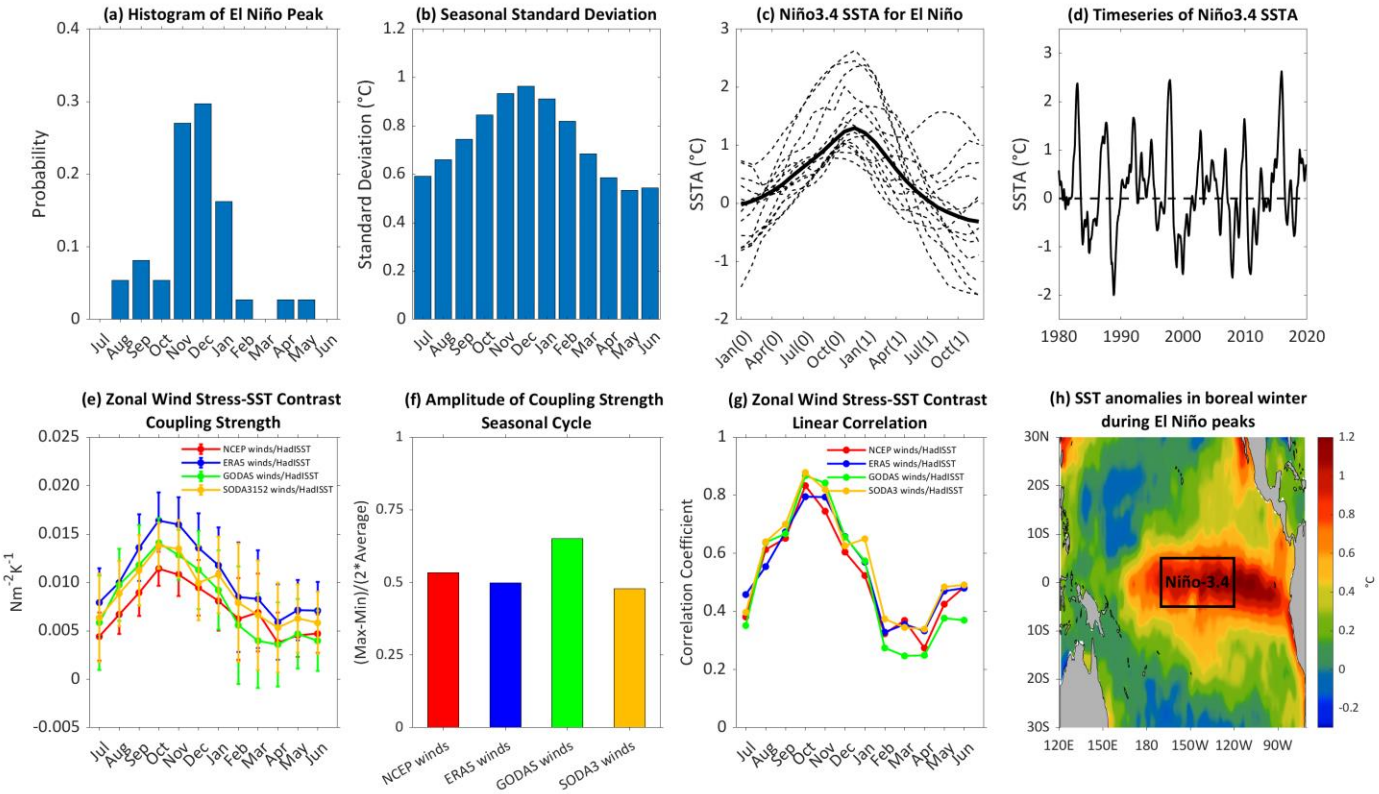

Figure 1. (a) Histogram of El Niño peak probabilities in 12 months (37 events). (b) Seasonal standard deviation of Niño-3.4 SSTA index. (c) Two-year segments of Niño-3.4 SSTA index for El Niño. (thick curve: composite mean, thin dashed curves: individual El Niño events over the past 50 years, Year(0): the former year, Year(1): the latter year). (d) A portion of the Niño-3.4 SSTA index timeseries (1980-2020). (e) Seasonal cycle of zonal wind stress-SST contrast coupling strength. Vertical error bars represent 95% confidence intervals for the linear regression coefficient (coupling strength). Colored curves represent results calculated from different datasets. (f) Amplitude of the coupling strength seasonal cycle (defined as half the maximum-minimum difference divided by the average). (g) Seasonal cycle of the linear correlation coefficients between the zonal wind stress and zonal SST contrast anomalies. (h) Tropical Pacific SSTA in boreal winter (Nov-Jan) during El Niño peaks (averaged for events over the past 50 years).

Figures 1a-1d illustrate the observed El Niño peak phase-locking characteristics via Niño-3.4 SSTA during 1870-2023. Figure 1a shows a histogram of El Niño peaks indicating that El Niño events tend to peak during boreal winter (November-January). Figure 1b shows that standard deviation shows a seasonal cycle with the peak in December and valley in May. Figure 1c depicts the composite evolution of El Niño (thick line) around the time it peaks; The averaged evolution peaks during boreal winter, which further demonstrates the phase-locking feature. Figure 1d shows the Niño-3.4 SSTA index timeseries, indicating the nonlinear characteristics of ENSO, such as irregularity and amplitude diversity.

Figures 1e-1g show the coupling strength calculated from datasets. The coupling strength shows a strong annual cycle (Figure 1e). The coupling strength reaches the maximum in October (boreal autumn) and decreases thereafter until it reaches the minimum in April (spring). The seasonal phases are highly consistent across datasets. Figure 1f presents the calculated seasonal cycle amplitude defined as (max minus min)/(2*mean). Three datasets (NCEP-NCAR Reanalysis 1, ERA5, and SODA 3.15.2) show an amplitude of 0.5, while GODAS dataset yields a higher value of 0.65. The coupling strength is strongest in boreal autumn and weakest in spring, while El Niño events tend to peak during the intervening winter months. Figure 1g shows the seasonal cycle of the zonal wind stress-zonal SST gradient correlation, with the strongest/weakest correlation in October/February-April and high consistency across different datasets. This suggests that in boreal spring, the weaker response of wind stress to SST anomalies may be due to a lower correlation between the two. Calculation details of the seasonal cycles of coupling strength and correlation coefficient are in the scatter plots for zonal SST gradient and zonal wind stress anomalies in 12 months shown in Supporting Information (Figure S1). Figure 1h shows the SST anomaly spatial distribution at the peak of El Niño during boreal winter, with warm SST anomalies concentrated in the central and eastern equatorial Pacific. The black box highlights the Nino-3.4 region.

3.2 Phase-locking of El Niño peaks simulated by the model with coupling strength seasonal cycle

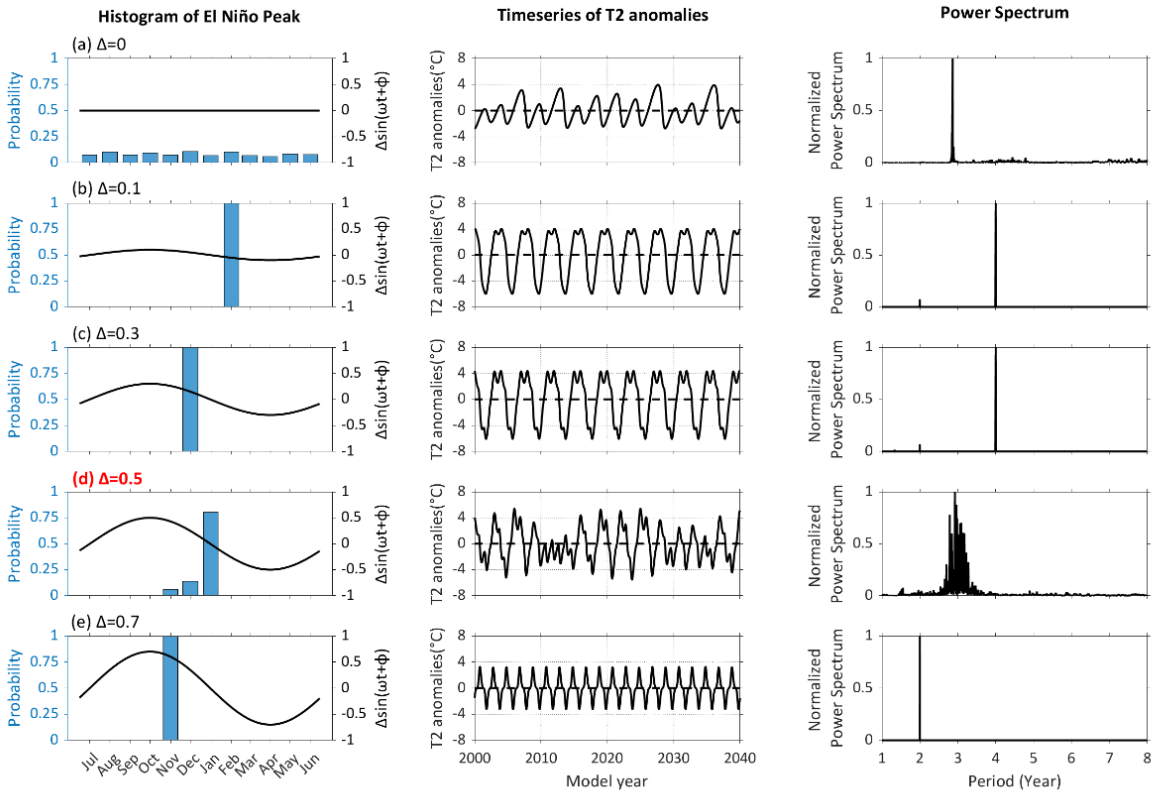

Figure 2. (left) Histograms of El Niño Peak from experiments with the increasing amplitudes of coupling strength seasonal cycle (Δ). (a) Δ=0 (annual mean case), (b) Δ=0.1, (c) Δ=0.3, (d) Δ=0.5 (red bold font, observations), (e) Δ=0.7. The phase is fixed at ϕ=335π/365 (maximum/minimum in October/April). (middle) and (right) are 40-yr portions and the power spectrum of T_2 anomaly timeseries from each experiment.

Figure 2 shows the experiments where the coupling strength seasonal cycle is incorporated into the model, with its amplitude gradually increased. The maximum/minimum coupling strength is in October/April as observed. When the amplitude approaches the observed value ((d) $\Delta = 0.5$), the El Niño peaks lock to boreal winter (November-January). This demonstrates that incorporating the observed coupling strength seasonal cycle effectively simulates the phase-locking characteristics. Additionally, T_2 anomalies timeseries shows the diversity and decadal variability of ENSO amplitude, which is consistent with observations. In the frequency domain, the power spectrum displays a broadband distribution with prominent peaks at approximately 3-year period. Compared to the original model((a) Δ=0), the introduction of observed seasonal cycle improves the simulations in the frequency aspects.

Next, we examine the impacts of the seasonal cycle amplitude on the phase-locking strength. Without seasonal cycle, El Niño peaks distribute uniformly across months, indicating no phase-locking((a) Δ=0). When the seasonal cycle is introduced ((b) $\Delta = 0.1$ and (c) $\Delta = 0.3$), El Niño peaks are completely locked to one single month. As the seasonal cycle amplitude increases to 0.5 (d), the phase-locking weakens, with peak-time across November-January. With further

increases in amplitude ((e) $\Delta = 0.7$), all El Niño peaks again align within one single month. These results illustrate that the phase-locking dues to the nonlinear frequency locking of ENSO to the seasonal cycle (Jin et al., 1994, 1996; Stein et al., 2014). Experiments (b), (c), and (e) yield frequency-locked solutions with strictly periodic oscillations, where ENSO frequency is a rational multiple of the seasonal cycle. In (b) and (c), the power spectrum shows the 4-year ENSO period, while (e) shows the 2-year period, causing all El Niño events to peak in one month. Experiment (d) represents the chaotic situation where irregular shifts between frequency-locked solutions cause El Niño to peak in several consecutive months instead of locking in one month. However, these shifts do not move the peaks to other seasons, all peaks remain in boreal winter. When $\Delta = 0.9$, ENSO is suppressed, leaving only seasonal frequency in the forced system (Chang et al., 1994). This result is in the Figure S2 in the Supporting Information.

These findings highlight that the amplitude of the coupling strength seasonal cycle modulates the strength of phase-locking. Besides, the variation amplitude of the seasonal standard deviation of T_2 increases with the seasonal cycle amplitude, further demonstrating its modulating effect on phase-locking strength. Seasonal std and trajectory of the system, projected onto the plan of T_2 and h_1' are in the Figure S3 in the Supporting Information.

Then, we discuss the influence of the seasonal cycle amplitude on the timing of El Niño phase-locking. As shown in Figure 2 and Figure S3, El Niño events tend to peak within boreal winter in all the experiments where the coupling strength seasonal cycle is incorporated (Experiments (b)-(e)). However, as the seasonal cycle amplitude varies, the time lag between the peak in coupling strength and the El Niño peak shifts, affecting the timing of phase-locking. In Experiment (b), with a relatively low seasonal cycle amplitude, this lag is about four months, placing the peak in February. As the seasonal amplitude increases in (c) and (d), the lag shortens to 2-3 months, shifting the peak to December-January. In (e), the peak is further advanced to November with an even larger seasonal amplitude.

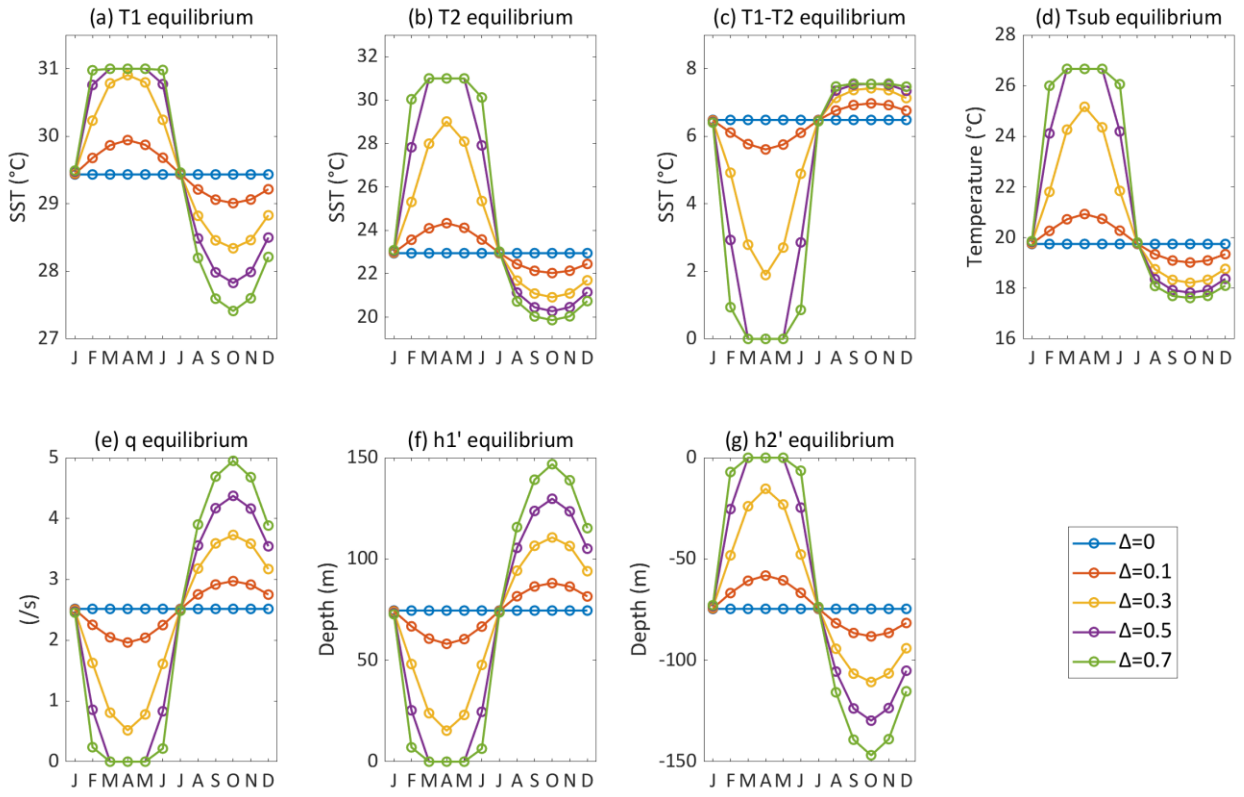

Figure 3. Equilibrium values as a function of coupling strength across the seasonal cycle. (a) the western equatorial Pacific (WEP) SST, T_1; (b) the eastern equatorial Pacific (EEP) SST, T_2; (c) zonal SST contrast T_1-T_2; (d) subsurface temperature T_{sub}; (e) upwelling q; (f) WEP thermocline depth h_1'; (g) EEP thermocline depth h_2'. Curves in different colors represent different seasonal cycle amplitudes. The equilibria are calculated at fixed coupling strength of each month in the seasonal cycle.

Previous studies have shown that the phase-locking of El Niño peaks is dominated by the seasonal cycle of ENSO growth rate (Chen & Jin, 2020, 2022; Stein et al., 2010, 2014). Figure 3 shows equilibrium states of the model as a function of coupling strength across the seasonal cycle. It can be seen that in the boreal autumn (strong coupling strength), WEPSST (T_1) and EEPSST (T_2) get colder in Figure 3a-3b. The zonal SST contrast increases because EEPSST decreases faster in Figure 3c. The wind stress is strengthened, and the upwelling (q) is stronger in Figure 3e. More heat content accumulates in the upper layer of the WP to form a deeper thermocline depth (h_1') in Figure 3f. In the EP, the thermocline depth (h_2') is shallower (Figure 3g) with colder subsurface temperature (Figure 3d). The situations in autumn may represent a higher ENSO growth rate. While in spring with the weakest coupling strength, the zonal contrast between the WP and EP becomes smaller in SST, thermocline depth (a more zonally symmetric equilibrium state) which represent a lower growth rate. Thus, introducing a seasonal cycle of coupling strength into the model may be equivalent to partially incorporating a seasonal cycle of ENSO growth rate into the recharge-discharge oscillator. The growth rate reaches maximum/minimum in autumn/spring, which is consistent with Chen & Jin (2020, 2022).

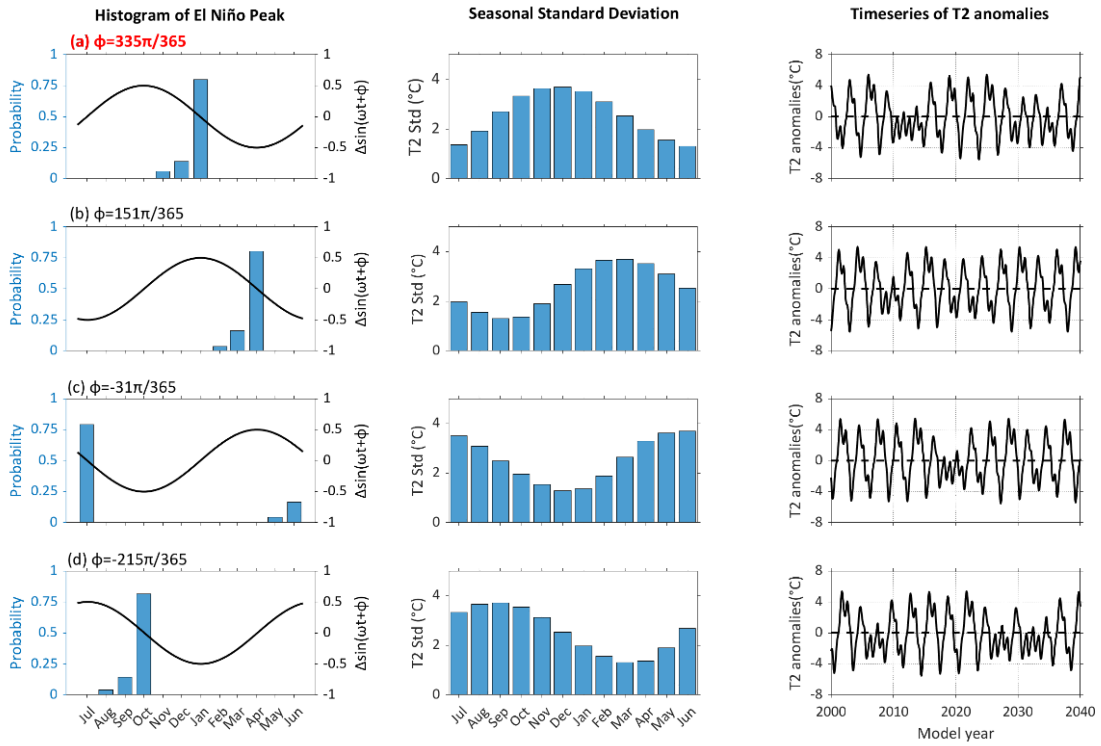

Figure 4. (left) Histograms of El Niño peak from experiments with varying phases of the coupling strength seasonal cycle (ϕ). (a) ϕ=335π/365 (max/min: Oct/Apr) consistent with observations. (b) ϕ=151π/365 (max/min: Jan/Jul). (c) ϕ=-31π/365 (max/min: April/Oct). (d) ϕ=-215π/365 (max/min: Jul/Jan). Amplitude of the seasonal cycle is fixed at Δ=0.5. (middle) and (right): seasonal standard deviations and 40-yr portions of the T_2 anomaly timeseries from each experiment.

Figure 4 shows the phase sensitivity experiments of the coupling strength seasonal cycle. The amplitude is fixed (Δ =0.5). In experiment (a) (the phase aligns with observations), El Niño peaks lock to boreal winter with a time lag of 2-3 months between the coupling strength peak and the El Niño event peak. In the other three experiments, when the phase ϕ is shifted, the locking season of El Niño peaks shifts correspondingly, and the time lag of 2-3 months remains consistent. In Experiment (b), the maximum/minimum coupling strength is in January/July, El Niño peaks lock in March-April (boreal spring). In (c), the maximum/minimum coupling strength is in April/October, El Niño peaks lock to June-July (boreal summer). In (d), the maximum/minimum coupling strength is in July/January, El Niño peaks lock to September-October (boreal autumn).

These findings indicate that the phase of the seasonal cycle in coupling strength primarily determines the timing of El Niño peaks, explaining that El Niño peaks in winter because the coupling strength is highest in October and lowest in April. Additionally, the phase of the seasonal cycle does not affect the strength of phase-locking.

The role of atmospheric thermal damping should be investigated through the same analysis as in part I. Firstly, the seasonal cycle is calculated from datasets, the damping coefficient is defined as the absolute value of the linear regression coefficients between net surface heating

and SST anomalies in eastern equatorial Pacific. The seasonal cycle is incorporated into the model through parameter *c*. Numerical experiments will be conducted to analyze the contribution to the phase-locking. The analysis will be presented in the second part of this study.

4 Conclusions and Discussion

The peak of El Niño has an important influence on global climate (Leung & Zhou, 2016; Li & Zhou, 2012; Zhang et al., 2022; Zhang et al., 2019). We use the model of Sun (1997) to study the phase-locking of El Niño peaks. The seasonal cycle of ocean-atmosphere coupling strength in the equatorial Pacific is calculated from datasets. Results reveal that the maximum/minimum coupling strength is in October/April, with an amplitude (half the difference between the maximum and minimum values relative to the mean) of approximately 0.5. Results from different datasets are highly consistent. Incorporating the observed seasonal cycle of coupling strength into the model well simulates the wintertime phase-locking of El Niño peaks, affirming the key role of coupling strength in this phenomenon. The simulated ENSO timeseries replicates the observed irregularity and decadal variability. Amplitude sensitivity experiments of the seasonal cycle reveal that the strength of phase-locking is significantly influenced by seasonal cycle amplitude through nonlinear frequency-locking of ENSO to the seasonal cycle. While changes in the seasonal cycle amplitude do not alter the locking season, they affect the peak-time by modifying the time lag between the coupling strength peak and the El Niño peak. El Niño peaks occur in boreal winter because of phase of the coupling strength seasonal cycle (Maximum/Minimum in October/April). Furthermore, we found the higher coupling strength in the seasonal cycle may correspond to a higher ENSO growth rate by calculating the seasonal cycle of the equilibrium state of the model.

The important role of coupling strength in the phase-locking in this work aligns with Jin et al., (2019). The coupling strength is comparable to the thermocline positive feedback in that work which is one of the two factors dominating the seasonal cycle of ENSO growth rate. Furthermore, the other factor is the atmospheric thermal damping rate whose influence on the phase-locking will be investigated in the next part of our work.

However, our study has limitations. Firstly, only the seasonal cycle of coupling strength is introduced. The primary influence of coupling strength on the phase-locking may be amplified or weakened by other processes as shown in the linear theory (Chen & Jin, 2022; Jin et al., 2020). It is better to calculate the seasonality of each parameter and investigate their contributions to the phase-locking. For now, since other processes modify the influence of coupling strength, we have conducted the amplitude/phase sensitivity experiments of the coupling strength seasonal cycle. All the experiments show the robust phase-locking of El Niño peaks. Secondly, the introduction of coupling strength in this study causes the annual cycle in upwelling/zonal current to have the same phase and amplitude as the seasonal cycle in coupling strength. This hypothesis is not consistent with observations. Further work needs to add the coupling strength seasonal cycle to the model from different positions respectively to study their contributions to seasonal phase-locking. Thirdly, when the amplitude of seasonal cycle is 0.5 corresponding to the observation, the equilibrium state and the standard deviation of EP SSTA show a much stronger seasonal variation than observations. For example, the T_2 equilibrium has the maximum/minimum value of 31°C /20°C in Apr/Oct (Figure 3b), while in observations the maximum/minimum value of the climatological state of EP SST is 27.5°C/24°C.

This difference may be due to that the annual mean state in the study is in the self-sustained regime with ENSO amplitude close to the real world, while researches utilize observations to show that the annual mean ENSO growth rate is slightly negative/positive near zero (not consider the seasonal cycle) (Chen & Jin, 2022; Jin et al., 2020; Xie & Jin, 2018). The parameter setting of the annual mean state here is consistent with Liang et al., (2012, 2017) and the annual mean does not change the role of coupling strength in phase-locking. However, future work needs to recalculate the annual mean state from observations. Moreover, it is found that the peak month of El Niño shifts within the boreal winter when the seasonal cycle amplitude varies, the mechanism for the shift needs to be investigated in future work.

Acknowledgments

This research was supported by the National Natural Science Foundation of China under grant 42250710154 and 42192563.

Open Research

The data is accessed through Behringer, D.W. et al. (1998) for the Global Ocean Data Assimilation System (GODAS) dataset. The data from the Simple Ocean Data Assimilation (SODA) 3.15.2 dataset is obtained through Carton et al. (2018). The fifth-generation ECMWF atmospheric reanalysis of the global climate (ERA5) dataset is obtained through Hersbach et al. (2020). The NCEP-NCAR Reanalysis 1 dataset is through Kalnay et al. (1996). The Hadley Centre Global Sea Ice and Sea Surface Temperature dataset (HadISST) is through Rayner et al. (2003).

References

Behringer, D. W., Ji, M., & Leetmaa, A. (1998). An Improved Coupled Model for ENSO Prediction and Implications for Ocean Initialization. Part I: The Ocean Data Assimilation System. *Monthly Weather Review*, *126*(4), 1013–1021. https://doi.org/10.1175/1520-0493(1998)126<1013:AICMFE>2.0.CO;2

Carton, J. A., Chepurin, G. A., & Chen, L. (2018). SODA3: A New Ocean Climate Reanalysis. *Journal of Climate*, *31*(17), 6967–6983. https://doi.org/10.1175/JCLI-D-18-0149.1

Chang, P., Wang, B., Li, T., & Ji, L. (1994). Interactions between the seasonal cycle and the Southern Oscillation - Frequency entrainment and chaos in a coupled ocean-atmosphere model. *Geophysical Research Letters*, *21*(25), 2817–2820. https://doi.org/10.1029/94GL02759

Chen, H.-C., & Jin, F.-F. (2020). Fundamental Behavior of ENSO Phase Locking. *Journal of Climate*, *33*(5), 1953–1968. https://doi.org/10.1175/JCLI-D-19-0264.1

Chen, H.-C., & Jin, F.-F. (2021). Simulations of ENSO Phase-Locking in CMIP5 and CMIP6. *Journal of Climate* , *34*. https://doi.org/10.1175/JCLI-D-200874.s1.

Chen, H.-C., & Jin, F.-F. (2022). Dynamics of ENSO Phase–Locking and Its Biases in Climate Models. *Geophysical Research Letters*, *49*(3), e2021GL097603. https://doi.org/10.1029/2021GL097603

Cheung, P. K. Y., Leung, M. Y. T., & Zhou, W. (2021). Position, Magnitude, and Size of Warm-Pool El Niño: Variability, Seasonal Predictability, and Climate Impacts. *Journal of Geophysical Research: Atmospheres*, *126*(14), e2021JD034917. https://doi.org/10.1029/2021JD034917

Galanti, E., & Tziperman, E. (2000). ENSO's Phase Locking to the Seasonal Cycle in the Fast-SST, Fast-Wave, and Mixed-Mode Regimes. *Journal of the Atmospheric Sciences*, *57*(17), 2936–2950. https://doi.org/10.1175/1520-0469(2000)057<2936:ESPLTT>2.0.CO;2

Hersbach, H., Bell, B., Berrisford, P., Hirahara, S., Horányi, A., Muñoz-Sabater, J., Nicolas, J., Peubey, C., Radu, R., Schepers, D., Simmons, A., Soci, C., Abdalla, S., Abellan, X., Balsamo, G., Bechtold, P., Biavati, G., Bidlot, J., Bonavita, M., … Thépaut, J.-N. (2020). The ERA5 global reanalysis. *Quarterly Journal of the Royal Meteorological Society*, *146*(730), 1999–2049. https://doi.org/10.1002/qj.3803

Hirst, A. C. (1986). Unstable and Damped Equatorial Modes in Simple Coupled Ocean-Atmosphere Models. *Journal of the Atmospheric Sciences*, *43*(6), 606–632. https://doi.org/10.1175/1520-0469(1986)043<0606:UADEMI>2.0.CO;2

Jian, Y., Leung, M. Y. T., Zhou, W., Jian, M., Yang, S., & Lin, X. (2021). Interdecadal Shift of the Relationship between ENSO and Winter Synoptic Temperature Variability over the Asian–Pacific–American Region in the 1980s. *Journal of Climate*, *34*(13), 5321–5335. https://doi.org/10.1175/JCLI-D-20-0931.1

Jin, F.-F. (1996). Tropical Ocean-Atmosphere Interaction, the Pacific Cold Tongue, and the El Niño-Southern Oscillation. *Science, New Series*, *274*(5284), 76–78.

Jin, F.-F., Chen, H.-C., Zhao, S., Hayashi, M., Karamperidou, C., Stuecker, M. F., Xie, R., & Geng, L. (2020). Simple ENSO Models. In *El Niño Southern Oscillation in a Changing Climate* (pp. 119–151). American Geophysical Union (AGU). https://doi.org/10.1002/9781119548164.ch6

Jin, F.-F., Neelin, J. D., & Ghil, M. (1994). El Niño on the Devil's Staircase: Annual Subharmonic Steps to Chaos. *Science*, *264*(5155), 70–72. https://doi.org/10.1126/science.264.5155.70

Jin, F.-F., Neelin, J. D., & Ghil, M. (1996). El Niño/Southern Oscillation and the annual cycle: Subharmonic frequency-locking and aperiodicity. *Physica D: Nonlinear Phenomena*, *98*(2–4), 442–465. https://doi.org/10.1016/0167-2789(96)00111-X

Jin, Y., Liu, Z., Lu, Z., & He, C. (2019). Seasonal Cycle of Background in the Tropical Pacific as a Cause of ENSO Spring Persistence Barrier. *Geophysical Research Letters*, *46*(22), 13371–13378. https://doi.org/10.1029/2019GL085205

Kalnay, E., Kanamitsu, M., Kistler, R., Collins, W., Deaven, D., Gandin, L., Iredell, M., Saha, S., White, G., Woollen, J., Zhu, Y., Leetmaa, A., Reynolds, B., Chelliah, M., Ebisuzaki, W., Higgins, W., Janowiak, J., Mo, K. C., Ropelewski, C., … Joseph, D. (1996). The NCEP/NCAR 40-Year Reanalysis Project. *Bulletin of the American Meteorological Society*, *77*, 437–472. https://doi.org/10.1175/1520-0477(1996)077<0437:TNYRP>2.0.CO;2

Kim, B.-M., & An, S.-I. (2011). Understanding ENSO Regime Behavior upon an Increase in the Warm-Pool Temperature Using a Simple ENSO Model. Journal of Climate, 24(5), 1438–1450. https://doi.org/10.1175/2010JCLI3635.1

Leung, M. Y. T., & Zhou, W. (2016). Direct and indirect ENSO modulation of winter temperature over the Asian–Pacific–American region. *Scientific Reports*, *6*(1), 36356. https://doi.org/10.1038/srep36356

Li, R. C. Y., & Zhou, W. (2012). Changes in Western Pacific Tropical Cyclones Associated with the El Niño–Southern Oscillation Cycle. *Journal of Climate*, *25*(17), 5864–5878. https://doi.org/10.1175/JCLI-D-11-00430.1

Liang, J., Yang, X.-Q., & Sun, D.-Z. (2012). The Effect of ENSO Events on the Tropical Pacific Mean Climate: Insights from an Analytical Model. *Journal of Climate*, *25*(21), 7590–7606. https://doi.org/10.1175/JCLI-D-11-00490.1

Liang, J., Yang, X.-Q., & Sun, D.-Z. (2017). Factors Determining the Asymmetry of ENSO. *Journal of Climate*, *30*(16), 6097–6106. https://doi.org/10.1175/JCLI-D-16-0923.1

Philander, S. G. H. (1989). El Niño, La Niña, and the southern oscillation. *El Niño, La Niña, and the Southern Oscillation*, *46*, [300 p.].

Philander, S. G. H., Yamagata, T., & Pacanowski, R. C. (1984). Unstable Air-Sea Interactions in the Tropics. *Journal of the Atmospheric Sciences*, *41*(4), 604–613. https://doi.org/10.1175/1520-0469(1984)041<0604:UASIIT>2.0.CO;2

Rayner, N. A., Parker, D. E., Horton, E. B., Folland, C. K., Alexander, L. V., Rowell, D. P., Kent, E. C., & Kaplan, A. (2003). Global analyses of sea surface temperature, sea ice, and night marine air temperature since the late nineteenth century. *Journal of Geophysical Research: Atmospheres*, *108*(D14). https://doi.org/10.1029/2002JD002670

Roberts, A., Guckenheimer, J., Widiasih, E., Timmermann, A., & Jones, C. K. R. T. (2016). Mixed-Mode Oscillations of El Niño–Southern Oscillation. Journal of the Atmospheric Sciences, 73(4), 1755–1766. https://doi.org/10.1175/JAS-D-15-0191.1

Stein, K., Schneider, N., Timmermann, A., & Jin, F.-F. (2010). Seasonal Synchronization of ENSO Events in a Linear Stochastic Model*. *Journal of Climate*, *23*(21), 5629–5643. https://doi.org/10.1175/2010JCLI3292.1

Stein, K., Timmermann, A., Schneider, N., Jin, F.-F., & Stuecker, M. F. (2014). ENSO Seasonal Synchronization Theory. *Journal of Climate*, *27*(14), 5285–5310. https://doi.org/10.1175/JCLI-D-13-00525.1

Sun, D.-Z. (1997). El Niño: A coupled response to radiative heating? *Geophysical Research Letters*, *24*(16), 2031–2034. https://doi.org/10.1029/97GL01960

Sun, D.-Z., & Trenberth, K. E. (1998). Coordinated heat removal from the equatorial Pacific during the 1986–87 El Niño. Geophysical Research Letters, 25(14), 2659–2662. https://doi.org/10.1029/98GL01813

Sun, D.-Z. (2003). A Possible Effect of an Increase in the Warm-Pool SST on the Magnitude of El Niño Warming. *Journal of Climate*, *16*(2), 185–205. https://doi.org/10.1175/1520-0442(2003)016<0185:APEOAI>2.0.CO;2

Sun, D.-Z., & Liu, Z. (1996). Dynamic Ocean-Atmosphere Coupling: A Thermostat for the Tropics. *Science*. https://doi.org/10.1126/science.272.5265.1148

Sun, D.-Z., Zhang, T., & Shin, S.-I. (2004). The Effect of Subtropical Cooling on the Amplitude of ENSO: A Numerical Study. *Journal of Climate*, *17*(19), 3786–3798. https://doi.org/10.1175/1520-0442(2004)017<3786:TEOSCO>2.0.CO;2

Tian, Y., Zhou, W., Zhang, L., Zhang, Y., & Zhang, R. (2023). Changes in ENSO Modulation of the Distribution of Rapidly Intensifying Tropical Cyclones over the Western North Pacific in Boreal Autumn. *Journal of Climate*, *36*(22), 7739–7753. https://doi.org/10.1175/JCLI-D-23-0084.1

Timmermann, A., Jin, F.-F., & Abshagen, J. (2003). A Nonlinear Theory for El Niño Bursting. *Journal of the Atmospheric Sciences*, *60*(1), 152–165. https://doi.org/10.1175/1520-0469(2003)060<0152:ANTFEN>2.0.CO;2

Tu, S., Chan, J. C. L., Xu, J., & Zhou, W. (2022). Opposite Changes in Tropical Cyclone Rain Rate During the Recent El Niño and La Niña Years. *Geophysical Research Letters*, *49*(6), e2021GL097412. https://doi.org/10.1029/2021GL097412

Tziperman, E., Cane, M. A., Zebiak, S. E., Xue, Y., & Blumenthal, B. (1998). Locking of El Niño's Peak Time to the End of the Calendar Year in the Delayed Oscillator Picture of ENSO. *Journal of Climate*, *11*(9), 2191–2199. https://doi.org/10.1175/1520-0442(1998)011<2191:LOENOS>2.0.CO;2

Wang, W., Zhou, W., & Chen, D. (2014). Summer High Temperature Extremes in Southeast China: Bonding with the El Niño–Southern Oscillation and East Asian Summer Monsoon Coupled System. *Journal of Climate*, *27*(11), 4122–4138. https://doi.org/10.1175/JCLI-D-13-00545.1

Xie, R., & Jin, F.-F. (2018). Two Leading ENSO Modes and El Niño Types in the Zebiak–Cane Model. *Journal of Climate*, *31*(5), 1943–1962. https://doi.org/10.1175/JCLI-D-17-0469.1

Yan, B., & Wu, R. (2007). Relative Roles of Different Components of the Basic State in the Phase Locking of El Niño Mature Phases. *Journal of Climate*, *20*(16), 4267–4277. https://doi.org/10.1175/JCLI4242.1

Zebiak, S. E., & Cane, wM. A. (1987). A Model El Ni&ntilde–Southern Oscillation. *Monthly Weather Review*, *115*(10), 2262–2278. https://doi.org/10.1175/1520-0493(1987)115<2262:AMENO>2.0.CO;2

Zhang, R., Zhou, W., Tian, W., Zhang, Y., Liu, Z., & Cheung, P. K. Y. (2022). Changes in the Relationship between ENSO and the Winter Arctic Stratospheric Polar Vortex in Recent Decades. *Journal of Climate*, *35*(16), 5399–5414. https://doi.org/10.1175/JCLI-D-21-0924.1

Zhang, Y., Zhou, W., & Leung, M. Y. T. (2019). Phase relationship between summer and winter monsoons over the South China Sea: Indian Ocean and ENSO forcing. *Climate Dynamics*, *52*(9), 5229–5248. https://doi.org/10.1007/s00382-018-4440-8